ACS OMEGA

http://pubs.acs.org/journal/acsodf

Article

Potassium Poly(heptazine imide) Coupled with Ti_3C_2 MXene-Derived TiO_2 as a Composite Photocatalyst for Efficient Pollutant Degradation

Binbin Chen, Weiwei Lu,* Peng Xu, and Kaisheng Yao

Cite This: *ACS Omega* 2023, 8, 11397−11405

Read Online

ACCESS | Metrics & More | Article Recommendations | Supporting Information

ABSTRACT: The photocatalytic degradation of pollutants is an effective and sustainable way to solve environmental problems, and the key is to develop an efficient, low-cost, and stable photocatalyst. Polymeric potassium poly(heptazine imide) (K-PHI), as a new member of the carbon nitride family, is a promising candidate but is characterized by a high charge recombination rate. To solve this problem, K-PHI was in-situ composited with MXene Ti_3C_2-derived TiO_2 to construct a type-II heterojunction. The morphology and structure of composite K-PHI/TiO_2 photocatalysts were characterized via different technologies, including TEM, XRD, FT-IR, XPS, and UV−vis reflectance spectra. Robust heterostructures and tight interactions between the two components of the composite were verified. Furthermore, the K-PHI/TiO_2 photocatalyst showed excellent activity for Rhodamine 6G removal under visible light illumination. When the weight percent of K-PHI in the original mixture of K-PHI and Ti_3C_2 was set to 10%, the prepared K-PHI/TiO_2 composite photocatalyst shows the highest photocatalytic degradation efficiency as high as 96.3%. The electron paramagnetic resonance characterization indicated that the ·OH radical is the active species accounting for the degradation of Rhodamine 6G.

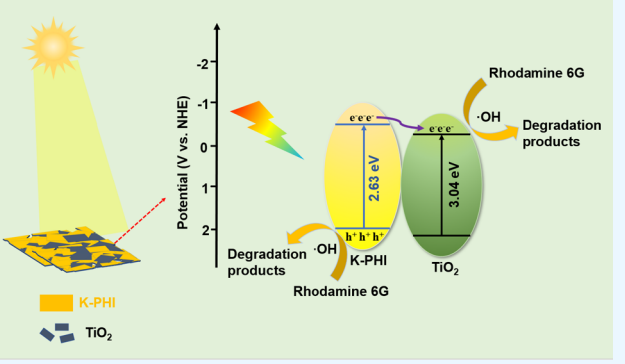

1. INTRODUCTION

The continuous development of industrialization and urbanization leads to more and more organic pollutants being discharged into the water environment. Therefore, the degradation of organic pollutants is particularly urgent for aqueous environmental protection. While tremendous efforts using techniques such as adsorption, membrane process, biodegradation, and electrochemical degradation have been used to solve water pollution problems, none of the available technologies to date provide a satisfactory solution due to their low efficiency, incapacity of mineralization, and high cost.[1−6] Photocatalytic degradation technology otherwise is characterized by mild reaction conditions, and the direct utilization of renewable solar energy is beneficial for energy saving and pollution control.[7−11] The key of photodegradation technology fundamentally requires the development of stable, efficient, and low-cost photocatalysts.[12]

In recent years, two-dimensional (2D) carbon nitride (CN) photocatalysts, such as α-C_3N_4, β-C_3N_4, and g-C_3N_4 have been widely used owing to their chemical stability, structural tunability, and facile synthesis from low-cost and abundant precursors.[13−15] Therefore, many studies have focused on the use of CN materials in the fields of photocatalytic water splitting and photodegradation of organic pollutants.[16,17] Moreover, in order to improve the catalytic activity of bulk C_3N_4, the preparation of mesoporous graphitic carbon nitride (mpg-C_3N_4) and the formation of a heterojunction composite are developed.[18,19] However, the conventional CN is limited by its slow charge transport, high recombination rate, and poor dispersion, which substantially damage its photocatalytic performance.[20]

Recently, poly (heptazine imide) (PHI) has stood out as a new member of the CN family.[21−25] The interesting aspect of PHI is that each heptazine unit in PHI is connected to three secondary amines, which obviously differs from conventional CNs. In addition, unlike traditional CN materials, PHI can promote electrical conduction and accelerate charge transport by introducing the desired metal cations.[26−28] Recent studies have found that alkali ion-doped PHI exhibited enhanced photocatalytic activity, owing to improved charge carrier separation and migration properties.[29,30] For example, potassium poly(heptazine imide) (K-PHI) with good photocatalytic activity was obtained through the substitution of 1, 2,

Received: January 9, 2023
Accepted: March 9, 2023
Published: March 20, 2023

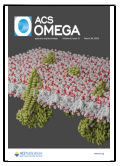

4-triazole derivatives via heating in LiCl/KCl eutectic, where the negative PHI 2D-layers were charge-compensated by K^+ cations.[31] The molten salt drove the interunit arrangement by increasing the intermolecular forces. More interestingly, the polymer can intercalate free ions from molten salts, which will strengthen the frameworks of polymer crystals.[32] Despite that PHI is highly attractive in the field of photocatalysis because of its unique structure, tunable optical property, and high charge transport nature, its fast photogenerated electron−hole recombination rate restricts its photocatalytic performance.[33]

In recent years, 2D MXene, as a precursor of in-situ formed TiO_2, is used to form heterojunction composites with other photoactive materials to improve the overall photocatalytic performance.[34−40] Studies have shown that Ti_3C_2 nanosheets are unstable and can be transformed into semiconductor TiO_2 in an oxidizing atmosphere.[41,42] For example, Gao et al.[42] prepared TiO_2/Ti_3C_2 heterojunction photocatalysts via an in situ hydrothermal method using MXene-Ti_3C_2 as the sole raw material. The TiO_2/Ti_3C_2 heterojunction photocatalysts demonstrated enhanced photocatalytic performance for CO_2 reduction. Yang et al.[36] reported that Ti_3C_2 was used as the TiO_2 precursor to construct a TiO_2/g-C_3N_4 photocatalyst, which exhibited an enhanced performance for photocatalytic hydrogen production. In addition, the obtained TiO_2 retained the 2D structure characteristics of MXene, which was beneficial to the photocatalytic reaction.[43,44] To the best of our knowledge, studies on the combination of MXene-derived TiO_2 with K-PHI to form a K-PHI/TiO_2 composite photocatalyst that are seldom reported.

In this study, to solve the problem of the high recombination rate for the PHI photocatalyst, an MXene-derived TiO_2-modified K-PHI composite (K-PHI/TiO_2) was successfully prepared and their photocatalytic performance was evaluated by degrading Rhodamine 6G dye. Rhodamine 6G is selected as a representative pollutant because it is a kind of industrial synthetic dye that is widely used in the printing, dyeing, and paper industry. It has been reported that skin contact with Rhodamine dyes or human ingestion of the substance will cause chronic or acute poisoning. In addition, animal experiments have found that Rhodamine dyes can induce cell cancerization or deformity.[45]

First, K-PHI/TiO_2 was prepared by a facile in-situ compositing method, in which the MXene-Ti_3C_2 was used as a natural Ti resource to generate TiO_2. Then, several characterizations, such as TEM, XRD, FT-IR, XPS, and UV−vis, were performed to determine the morphology, composite structure, and band structure. The characterization results confirmed the robust heterostructures and tight interactions between the two components of K-PHI and TiO_2. Then, the photocatalytic performance of K-PHI/TiO_2 for degradation of Rhodamine 6G is evaluated. The further mechanism investigation indicated that the construction of type-II heterojunction between K-PHI and TiO_2 accounts for the high photocatalytic activity of the composite.

2. EXPERIMENTAL SECTION

2.1. Chemicals and Materials. In this study, 3-amino-1,2,4-triazole-5-thiol ($C_2H_4N_4S$, ≥98%), lithium fluoride (LiF, ≥99%), potassium chloride (KCl, ≥99%), lithium chloride (LiCl, ≥99%), titanium aluminum carbide (Ti_3AlC_2), and Rhodamine 6G (≥95%) were purchased from Shanghai Aladdin Biochemical Technology Co. Ltd. Hydrochloric acid (HCl) was provided by Sinopharm.

2.2. Synthesis of K-PHI, Ti_3C_2, and K-PHI/TiO_2. K-PHI was synthesized via a bottom-up ionic thermal method using triazole as the precursor.[31] First, 3-amino-1,2,4-triazole-5-thiol (0.9 g) was mixed with salts of LiCl (2 g) and KCl (2.5 g) and then fully ground. Subsequently, the mixture was heated under a nitrogen atmosphere at 550 °C for 5 h. After the samples were cooled down, they were washed with deionized water and filtered, and this purification process was done additionally four times. At last, the samples were dried in a vacuum oven overnight at 50 °C to finally obtain the K-PHI products.

Layered Ti_3C_2 was prepared via the etching−intercalation method using Ti_3AlC_2 as the precursor.[46] First, LiF (1.6 g) was slowly added to 36% HCl (20 mL), and then, Ti_3AlC_2 (1 g) powder was slowly added to the mixture. Afterward, the obtained black solution was centrifuged for 24 h at 45 °C and washed repeatedly with dilute hydrochloric acid. The solution was then repeatedly washed with deionized water and centrifuged to a pH of 6. The suspension was sonicated for 2 h (ice bath) and then centrifuged for 30 min at 3500 rpm. The final collected suspension was freeze-dried and collected.

For synthesis of K-PHI/TiO_2 photocatalysts, a certain amount of K-PHI and Ti_3C_2 and several drops of alcohol were mixed and then fully ground. Afterward, the mixture of K-PHI and Ti_3C_2 was treated at 450 °C for 4 h. This heat treatment allows the in-situ transformation of Ti_3C_2 to TiO_2 and then closely contacts with K-PHI to finally obtain the K-PHI/TiO_2 composites. The weight percent of K-PHI in the original mixture of K-PHI and Ti_3C_2 was set to 5, 10, 20, and 25%, and these final K-PHI/TiO_2 samples are denoted as 5 K-PHI/TiO_2, 10 K-PHI/TiO_2, 20 K-PHI/TiO_2, and 25 K-PHI/TiO_2, respectively. For control, pristine K-PHI and TiO_2 were also prepared under the same heat treatment condition.

2.3. Characterizations. The scanning transmission electron microscopy−high-angle annular dark-field (STEM-HAADF) and energy-dispersive X-ray spectroscopy images were recorded using a field-emission scanning transmission electron microscope (HD-2300A, Hitachi Ltd., Japan). X-ray diffraction (XRD) spectra were measured using an X-ray diffractometer (Bruker D8 Advance). The ultraviolet−visible (UV−vis) spectra of K-PHI and K-PHI/TiO_2 samples were recorded using a UV−vis spectrophotometer (Persee, TU-1900, Beijing Persee Instruments Co., China). The Fourier-transform infrared (FT-IR) spectra were collected on a Nicolet 6700 spectrometer (Thermo Fisher Scientific Inc., USA). X-ray photoelectron spectroscopy (XPS) was conducted using an X-ray photoelectron spectrometer (Thermo Fisher, ESCALAB 250Xi, USA). Electron paramagnetic resonance (EPR) spectra for detection of reactive species were collected using a spectrometer (Bruker, A300, Germany) equipped with a cylindrical resonator. The mineralization degree of Rhodamine 6G was characterized by determining the total organic carbon (TOC) removed, which was determined using a Shimadzu TOC-L (Japan). The photoluminescence (PL) spectra were evaluated on a fluorophotometer (Edinburgh FLS1000, Britain).

2.4. Photocatalytic Degradation Experiments. Photodegradation of Rhodamine 6G was performed in a cylindrical reactor, and the reaction temperature was controlled via water circulation through the outer jacket of the reactor. A 300 W xenon lamp with a 420 nm filter (filtering ultraviolet light) was used as a visible light source. The distance between the lamp and the reactor is approximately 1 cm. In the degradation reaction experiment, 100 mg of catalyst was added to 50 mL of

https://doi.org/10.1021/acsomega.3c00150
ACS Omega 2023, 8, 11397−11405

Scheme 1. Preparation Process of the K-PHI/TiO_2 Composite Samples

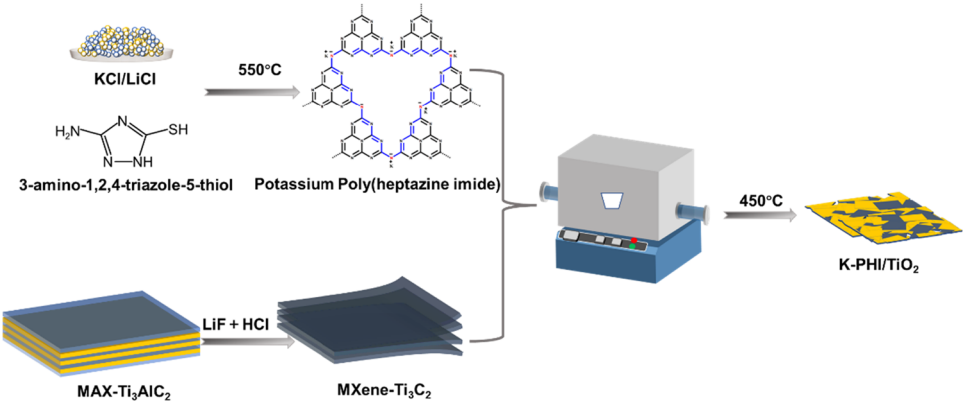

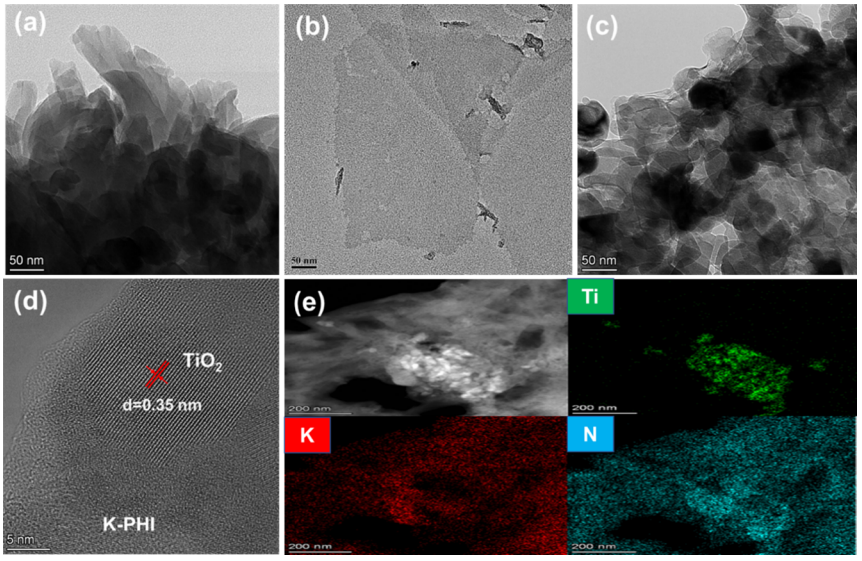

Figure 1. TEM images of K-PHI (a) and MXene (b) samples. TEM (c), high-resolution TEM, (d) and elemental mapping (e) of Ti, K, and N for the K-PHI/TiO_2 photocatalyst.

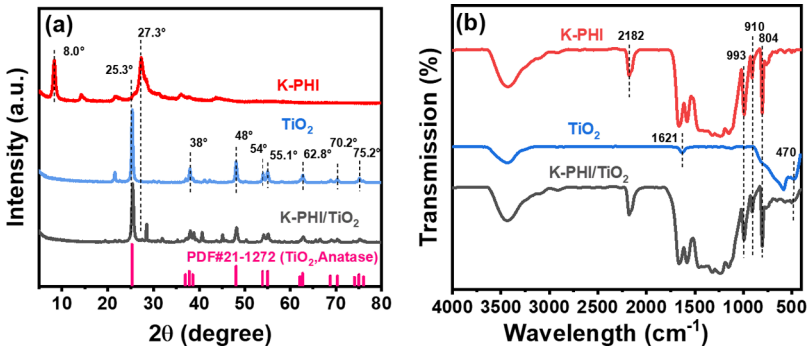

Figure 2. XRD patterns (a) and FTIR spectra (b) of K-PHI, TiO_2, and K-PHI/TiO_2 photocatalysts.

a Rhodamine 6G solution with a concentration of 20 mg/L, and the initial pH of the solution was ~7. The catalyst was stirred under dark conditions for 30 min to achieve full contact with Rhodamine 6G molecules and adsorption−desorption equilibrium. The reaction solution (1 mL) was taken at a fixed interval, and the catalyst was separated out via centrifugation. Then, the solution was analyzed by UV−vis to monitor the degradation process.

3. RESULTS AND DISCUSSION

3.1. Preparation and Characterization of K-PHI/TiO_2 Composite Samples. The overall preparation route of the K-PHI/TiO_2 composite is illustrated in Scheme 1. K-PHI was first synthesized via a bottom-up ionic thermal method, in which the precursor of 3-amino-1,2,4-triazole-5-thiol was heated in LiCl/KCl at 550 °C for 5 h.[31] Figure 1a shows the TEM image of K-PHI, and the K-PHI displayed a distinct sheet-like morphology. Ultrathin Ti_3C_2 nanosheets were

https://doi.org/10.1021/acsomega.3c00150
ACS Omega 2023, 8, 11397−11405

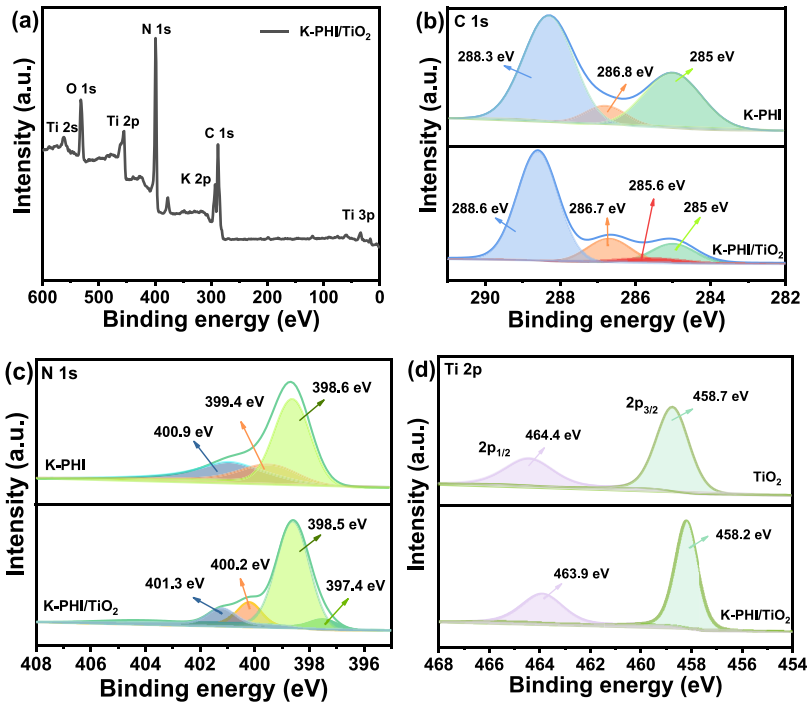

Figure 3. (a) Full survey spectrum of K-PHI/TiO_2; (b) C 1s spectra of K-PHI and K-PHI/TiO_2 photocatalysts; (c) N 1s spectra of K-PHI and K-PHI/TiO_2 photocatalysts; (d) Ti 2p spectra of TiO_2 and K-PHI/TiO_2 photocatalysts.

prepared via an etching−intercalation method, in which the accordion-like MAX-phase Ti_3AlC_2 was transformed to Ti_3C_2 nanosheets in the presence of HCl and LiF.[46,47] The TEM image in Figure 1b shows that the obtained Ti_3C_2 featured an ultrathin nanosheet morphology. Finally, for synthesis of the K-PHI/TiO_2 composite, the as-prepared K-PHI and Ti_3C_2 were fully mixed and ground and then heat-treated at 450 °C for 4 h. In this heat treatment process, the TiO_2 nanosheets were in situ formed from oxidation of Ti_3C_2 and composited with K-PHI to form K-PHI/TiO_2. Figure 1c depicts the microstructure of the formed K-PHI/TiO_2 composite. The K-PHI/TiO_2 composite exhibited an obvious sheet-like morphology with some amorphous structures owing to the lamellar nature of K-PHI. To further investigate the structure of the photocatalyst, the K-PHI/TiO_2 composite photocatalyst was analyzed via high-resolution TEM (Figure 1d). The HRTEM images showed the clear lattice fringes of the TiO_2 (101) plane with a spacing distance of 0.35 nm, and TiO_2 was in close contact with the component of K-PHI[43]. Moreover, the elemental mapping images (Figure 1e) showed that N, K, and Ti were well-defined, which confirms that TiO_2 was attached to K-PHI.

The XRD patterns of K-PHI, TiO_2, and K-PHI/TiO_2 are shown in Figure 2a. The K-PHI pattern featured two peaks, which indicates that triazole was successfully transformed into K-PHI. The strong peak at 27.3° corresponded to the (002) plane and resulted from the interlayer stacking structure of K-PHI.[31,48] The minor XRD peak at 8° is related to the $(\bar{1}10)$ plane, stemming from the increased in-plane periodicity of K-PHI[32]. The distinct diffraction peaks of TiO_2 at 2θ = 25.3, 38.0, 48.0, 54.0, 55.1, 62.8, 70.2, and 75.2° can be ascribed to the (101), (004), (200), (105), (211), (204), (116), and (220) planes of anatase TiO_2, respectively.[43] The obtained XRD patterns indicate that MXene-Ti_3C_2 was completely converted into the anatase phase of TiO_2 via calcination.[38,49] As for the K-PHI/TiO_2 sample, the XRD pattern contains the characteristic diffraction peaks of K-PHI and TiO_2. However, the XRD peak of K-PHI at 8° disappeared in that of K-PHI/TiO_2, and this is because the structure in the periodic plane of K-PHI is disrupted during the in-situ composite of Ti_3C_2-dervied TiO_2 with K-PHI. In addition, compared with pure K-PHI, the (002) diffraction peak of K-PHI/TiO_2 shifted to the right to a certain extent, indicating that the interaction between the two components resulted in smaller packing distance and lower packing degree of K-PHI nanosheets.[43,50] These results demonstrate the successful formation of the K-PHI/TiO_2 heterojunction composite during the calcination of a mixture of K-PHI and MXene-Ti_3C_2.

The FTIR spectra of the prepared samples were further collected, and the results are shown in Figure 2b. From the FTIR spectrum of the K-PHI sample, several characteristic signals of K-PHI, such as the out-plane bending vibration of heptazine rings around 804 cm^{-1}, the vibration mode of the C−N at 910 and 993 cm^{-1}, and the stretching vibration of cyano units (C≡N) at 2182 cm^{-1}, can be observed.[51,52] The FTIR spectrum of Ti_3C_2-derived TiO_2 featured a peak of the stretching vibration mode of the Ti−O−Ti bond at ∼470 cm^{-1}. Another distinct peak at ∼1621 cm^{-1} that corresponded to O−H bending vibration of hydroxyl groups on the TiO_2 surface can also be observed.[20,53] From the FT-IR curve K-PHI/TiO_2, the characteristic peaks of K-PHI and TiO_2 can be observed, which substantiates the successful formation of the composite between K-PHI and TiO_2.

K-PHI/TiO_2 was further characterized via X-ray photoelectron spectroscopy (XPS). The resultant XPS curves and the corresponding devolution peaks for C 1s, N 1s, and Ti 2p are shown in Figure 3. The survey XPS spectrum of K-PHI/TiO_2 in Figure 3a shows that all signal peaks can be assigned to elements of Ti, O, N, K, and C, and no peaks of any other elements were observed. Figure 3b shows the C 1s XPS spectra

https://doi.org/10.1021/acsomega.3c00150
ACS Omega 2023, 8, 11397−11405

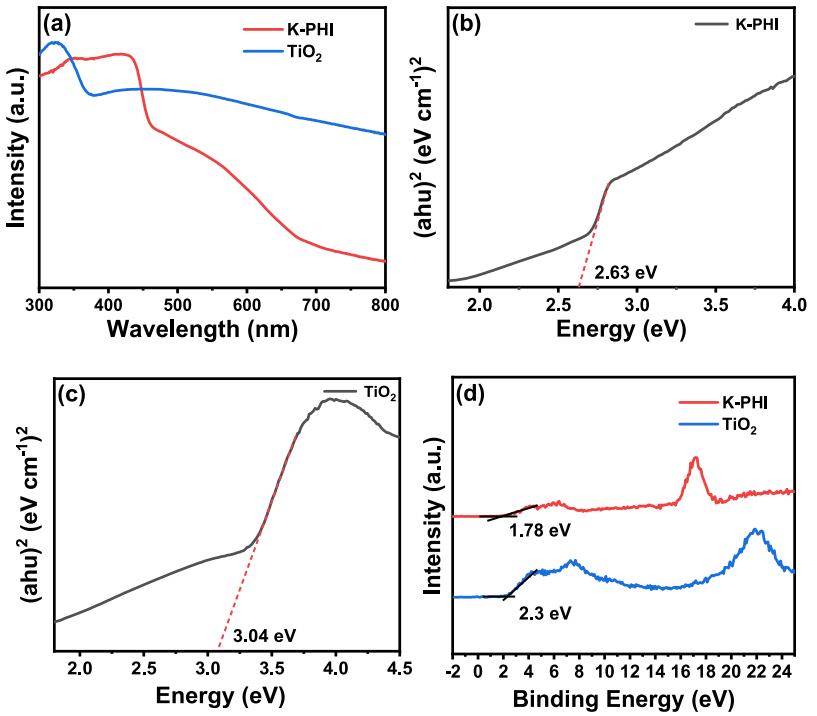

Figure 4. UV−vis diffused reflectance spectra of K-PHI and TiO_2(a); $(\alpha h\nu)^2$ vs $h\nu$ Tauc plots of K-PHI (b) and TiO_2(c); valence band XPS spectra of K-PHI and TiO_2 (d).

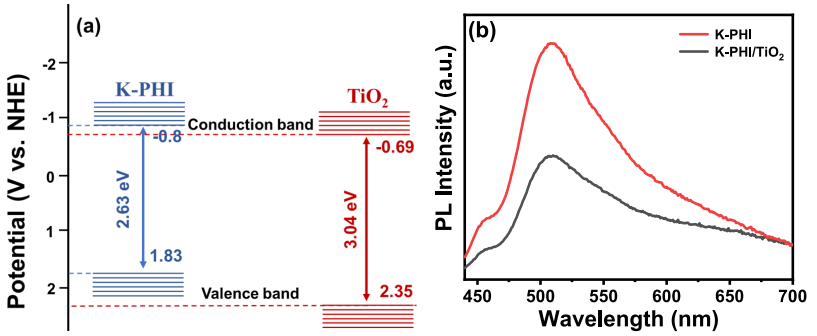

Figure 5. (a) Band structure of the K-PHI/TiO_2 composite photocatalyst; (b) PL spectra of K-PHI and K-PHI/TiO_2 photocatalysts.

of K-PHI and K-PHI/TiO_2. For the C 1s XPS spectrum of K-PHI, the peak with a binding energy (BE) of 288.3 eV is assigned to C from CN_3 bonds of the heterocycle ring; the peak at 286.8 eV corresponded to C from the hydroxylated surface carbon (C−OH), and the peak at 285 eV was related to the adventitious C[31]. For composite K-PHI/TiO_2, the BE of the adventitious carbon peak at 285 eV is the same as that of K-PHI. However, a new minor peak assigned to C−O appears in the spectrum of K-PHI/TiO_2, which may relate to the oxygen-containing groups of the calcination residue of Ti_3C_2. In addition, the C 1s peak of K-PHI/TiO_2 at 288.6 eV is 0.3 eV higher than that of the peak in the K-PHI spectrum, indicating the occurrence of electron transfer between the two constituents due to the formation of heterostructures.[34]

For the high-resolution XPS spectrum of N 1s (Figure 3c), the peaks at 398.6, 399.4, and 400.9 eV in the spectrum of K-PHI are attributable to the sp^2-hybridized N of the C═N−C, N−$(C)_3$, and N−H groups, respectively.[31] Compared with the N 1s XPS peaks of K-PHI, these three peaks of K-PHI/TiO_2 were shifted to higher BE regions, indicating that the electrons were transferred from K-PHI to TiO_2 through N−Ti interactions.[54] In addition, the K-PHI/TiO_2 spectrum featured a new peak related to Ti-N at 397.4 eV, confirming the formation of chemical bonds between K-PHI and TiO_2 during the thermal calcination process.

The Ti 2p XPS spectrum of the TiO_2 sample (Figure 3d) subjected to 4 h of calcination featured Ti−O bond XPS peaks at 458.7 and 464.4 eV, which corresponded to the Ti $2p_{3/2}$ and Ti $2p_{1/2}$ orbitals of TiO_2, respectively. This confirmed that the precursor of MXene-Ti_3C_2 can be successfully transformed into TiO_2 after calcination in air.[43] The Ti 2p spectra of composite K-PHI/TiO_2 were similar to those of the TiO_2 sample and featured peaks at 458.2 and 463.9 eV. However, both the Ti 2p XPS peaks of the K-PHI/TiO_2 sample shifted by 0.5 eV to a lower BE, which resulted from the change in the chemical environment of Ti after compositing between K-PHI and TiO_2.[50,55] The high-resolution K 2p XPS spectra of both K-PHI/TiO_2 and K-PHI (Figure S1) featured peaks at 292.9 and 295.7 eV, indicating the incorporation of potassium ions in the composites.[31] In summary, the obtained results from the XPS characterization verified the robust contact and interaction between the components of K-PHI and TiO_2,

https://doi.org/10.1021/acsomega.3c00150
ACS Omega 2023, 8, 11397−11405

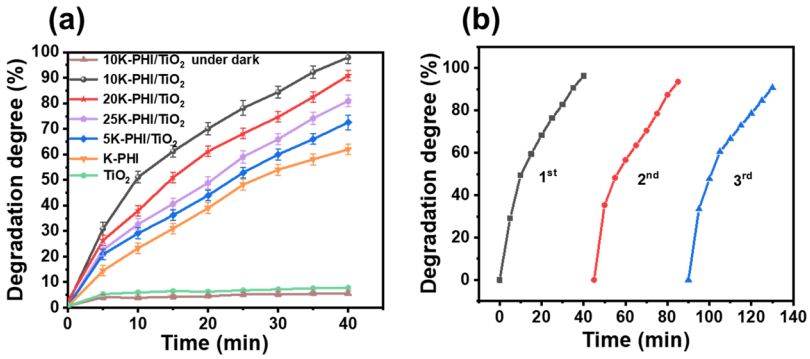

Figure 6. (a) Photocatalytic degradation curves of K-PHI/TiO_2 samples under visible light (λ > 420 nm) illumination. For control, the curves of pure K-PHI and TiO_2 are also included; (b) Reusability of the 10-K-PHI/TiO_2 composite photocatalyst for degradation of Rhodamine 6G.

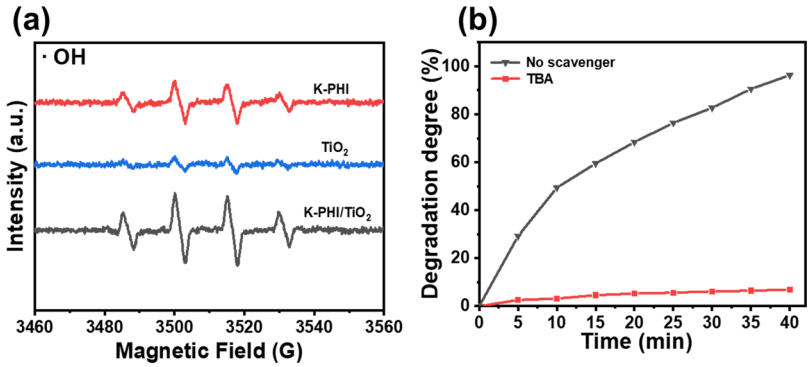

Figure 7. (a) Electron paramagnetic resonance spectra obtained in the presence of K-PHI, TiO_2, and K-PHI/TiO_2 under light illumination; (b) Degradation results when TBA was used as the trapping agent.

which will guarantee the facile transfer and enhanced separation of the charge carriers in the photocatalytic process.

3.2. Determination of Band Structures of K-PHI and TiO_2. After the structural characterization of the composite, the band structure of the sample was further determined. The UV−vis diffused reflectance spectroscopy of individual K-PHI and TiO_2 are shown in Figure 4a. From the corresponding Tauc plots (Figure 4b,c) of the UV−vis diffused reflectance spectra, the band gap (E_g) values of the K-PHI and TiO_2 were estimated. The obtained E_g values of K-PHI and TiO_2 were 2.63 and 3.04 eV, respectively. Then, the valence band (VB) edges of K-PHI and TiO_2 were determined via VB-XPS (Figure 4d). The values of the VB edge ($E_{VB\text{-}XPS}$) of K-PHI and TiO_2 are 1.78 and 2.3 eV, respectively. According to the equation $E_{VB\text{-}NHE} = \varphi + E_{VB\text{-}XPS} - 4.44$ (work function φ is 4.49), the VB edges relative to the normal hydrogen electrode ($E_{VB\text{-}NHE}$) of K-PHI and TiO_2 are 1.83 and 2.35 V (vs NHE), respectively. Then, following the formula $E_{CB\text{-}NHE} = E_{VB\text{-}NHE} - E_g$, the conduction band edge of K-PHI and TiO_2 were calculated to be −0.8 and −0.69 V (vs NHE), respectively.[56]

From these obtained $E_{VB\text{-}NHE}$, $E_{CB\text{-}NHE}$, and E_g, we can depict the band structure of the K-PHI/TiO_2 composite. As shown in Figure 5a, a type-II heterojunction was formed between K-PHI and TiO_2, in which the CB and VB positions of K-PHI straddled those of TiO_2. Thus, under light excitation, the photoinduced charge carriers of electrons on the CB of K-PHI could be facilely transferred to the CB of TiO_2, and TiO_2 acted as a sink of electrons, improving charge separation for the K-PHI/TiO_2 composite.[53,57] This charge separation effect can be proved by measuring the PL spectra of pure K-PHI and composite K-PHI/TiO_2 (see Figure 5b). It can be seen from Figure 5b that, compared with pure K-PHI, the PL intensity of composite K-PHI/TiO_2 is significantly decreased, indicating the efficient separation of photogenerated electrons and holes after the formation of composite between K-PHI and TiO_2.

3.3. Evaluation of the Photocatalytic Degradation Performance and Determination of Active Species. After the preparation and characterization of K-PHI/TiO_2 composites, their photocatalytic degradation performance was further investigated using Rhodamine 6G as a pollutant probe. Figure 6a shows the degradation curves of the composite photocatalysts as well as pure K-PHI and TiO_2. It was found that the Ti_3C_2-derived TiO_2 has negligible removal activity for the degradation of Rhodamine 6G because the wide-bandgap TiO_2 cannot be excited under visible light. Compared with pristine K-PHI, all the K-PHI/TiO_2 composites exhibit better degradation performance. Among the K-PHI/TiO_2 with different contents of K-PHI, 10 K-PHI/TiO_2 shows the highest degradation activity, and the degradation degree of Rhodamine 6G within 40 min reaches 96.3%. The reason may be that when the content of K-PHI is too low, the K-PHI in K-PHI/TiO_2 cannot provide sufficient photoinduced carriers, resulting in the reduced degradation rate for Rhodamine 6G; on the other hand, when the content of K-PHI is too high, the photoinduced electrons of K-PHI cannot be timely transferred into the insufficient amount of TiO_2, which may decrease the charge separation efficiency and lower the photodegradation activity. Furthermore, we find that the pH of the solution has a significant effect on the photodegradation efficiency (Figure S2). When the pH value (pH = 5 and 7) is nearby the pHzpc value (6.4) of 10 K-PHI/TiO_2, the balance between the absorption of dye and the production of active species can be

https://doi.org/10.1021/acsomega.3c00150
ACS Omega 2023, 8, 11397−11405

obtained to achieve the optimal degradation efficiency. In addition, to investigate the extent of dye mineralization in the photodegradation process, the TOC content of the dye solution was further determined. As an example, a typical TOC removal curve in the presence of the 10 K-PHI/TiO_2 photocatalyst is shown in Figure S3, which shows that Rhodamine 6G dye can be totally mineralized by the prepared composite photocatalyst after 60 min irradiation.

To investigate the stability of the prepared K-PHI/TiO_2 sample, recycling experiment was conducted, and the results are shown in Figure 6b. The results show that, after three cycles, the degradation degree of Rhodamine 6G slightly decreases from 96.3 to 90.8, and 94.3% of the degradation activity is still maintained. Further structural characterization (Figure S4) shows that the XRD pattern shows little changes after three cycles, and no new peaks appear, indicating the good structural stability of the composite sample.

Finally, to identify the active species accounting for the degradation of Rhodamine 6G in the presence of K-PHI/TiO_2, electron paramagnetic resonance tests were performed. The test result showed that ·OH was the main active species in degrading Rhodamine 6G (Figure 7a). To confirm this point, the trapping experiments that used TBA as the trapping agent of OH was carried out. The results in Figure 7b show that the degradation degree of Rhodamine 6G falls from 96.3 to 6.9%, when the trapping agent TBA was added, and this degradation degree value of 6.9% is close to the value of 5.0% under the dark condition. Therefore, both the EPR and trapping experiment indicated that the OH played a major role in the degradation process in the presence of K-PHI/TiO_2 photocatalysts. From comparison, the composite exhibited a stronger ·OH signal than pure K-PHI and TiO_2, which means that K-PHI/TiO_2 can produce more active species of ·OH to attack the pollutant and achieve higher activity.

3.4. Photocatalytic Mechanisms. According to the above characterization and performance test results, we propose the reaction mechanism of Rhodamine 6G degradation using the K-PHI/TiO_2 photocatalyst under light conditions (Figure 8).

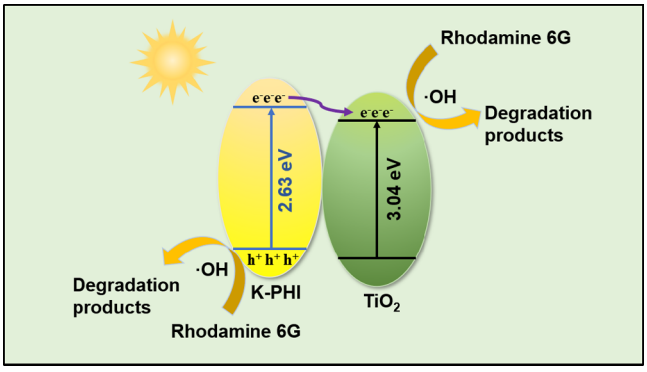

Figure 8. Proposed mechanism of the K-PHI/TiO_2 composite for the photocatalytic degradation of Rhodamine 6G.

Through in-situ transformation of MXene-Ti_3C_2 to TiO_2 under calcination, tight contact between K-PHI and TiO_2 can be formed, resulting in the successful preparation of a novel K-PHI/TiO_2 composite photocatalyst (see Figures 123). Under illumination of visible light, the K-PHI component in K-PHI/TiO_2 is excited to generate charge carriers of electrons and holes due to its narrow band gaps (see Figure 4). Subsequently, due to the suitable band structure of K-PHI and TiO_2 and the formed type-II heterostructure (see Figure 5a), the photoinduced electrons can facilely flow from the CB of K-PHI to that of TiO_2, in which TiO_2 acted as the electron sink. This oriented flow of electrons from K-PHI to TiO_2 effectively separates the photogenerated electrons and holes (see Figure 5b) and facilitates their immigration (see Figure S5). Next, the separated electrons and holes can generate highly reactive species of ·OH via various pathways (see Figure 7). At last, these reactive ·OH can unselectively attack and finally degrade the substrate of Rhodamine 6G.

4. CONCLUSIONS

Through in situ compositing method, an efficient K-PHI/TiO_2 composite was prepared using MXene-Ti_3C_2 as the precursor of TiO_2. This K-PHI/TiO_2 composite shows high efficiency for photocatalytic degradation of Rhodamine 6G. The enhanced activity of K-PHI/TiO_2 can be attributed to the following: (1) the in-situ transformation of MXene-Ti_3C_2 to TiO_2 and then compositing with K-PHI, leading to robust contact between K-PHI and TiO_2; (2) the formation of a type-II heterojunction between K-PHI and TiO_2, resulting in the promoted separation and the inhibited recombination of photogenerated charge carriers. This study provides a strategy for strengthening the heterostructure of non-metal PHI-based materials to develop efficient, low-cost, and environmentally friendly photocatalysts.

■ ASSOCIATED CONTENT

Supporting Information

The Supporting Information is available free of charge at https://pubs.acs.org/doi/10.1021/acsomega.3c00150.

K 2p spectra of K-PHI and K-PHI/TiO_2 photocatalysts; degradation curves of Rhodamine 6G in solutions with different pH values; TOC removal rate in solution under visible light irradiation; XRD patterns of the 10-K-PHI/TiO_2 sample before and after three cycles; and EIS pattern of K-PHI and K-PHI/TiO_2 (PDF)

■ AUTHOR INFORMATION

Corresponding Author

Weiwei Lu − *School of Chemical Engineering and Pharmaceutics, Henan University of Science and Technology, Luoyang, Henan 471003, China;* orcid.org/0000-0002-9940-5125; Email: luweiwei@haust.edu.cn

Authors

Binbin Chen − *School of Chemical Engineering and Pharmaceutics, Henan University of Science and Technology, Luoyang, Henan 471003, China*

Peng Xu − *School of Chemical Engineering and Pharmaceutics, Henan University of Science and Technology, Luoyang, Henan 471003, China*

Kaisheng Yao − *School of Chemical Engineering and Pharmaceutics, Henan University of Science and Technology, Luoyang, Henan 471003, China*

Complete contact information is available at: https://pubs.acs.org/10.1021/acsomega.3c00150

Notes

The authors declare no competing financial interest.

https://doi.org/10.1021/acsomega.3c00150
ACS Omega 2023, 8, 11397−11405

■ ACKNOWLEDGMENTS

This work was supported financially by the Key Scientific Research Projects of Higher Education Institutions in Henan Province (21A430015) and the National Natural Science Foundation of China (21673067).

■ REFERENCES

(1) Hassani, A.; Eghbali, P.; Mahdipour, F.; Wacławek, S.; Lin, K.-Y. A.; Ghanbari, F. Insights into the synergistic role of photocatalytic activation of peroxymonosulfate by UVA-LED irradiation over $CoFe_2O_4$-rGO nanocomposite towards effective Bisphenol A degradation: Performance, mineralization, and activation mechanism. *Chem. Eng. J.* **2023**, *453*, No. 139556.

(2) Yaghoot-Nezhad, A.; Wacławek, S.; Madihi-Bidgoli, S.; Hassani, A.; Lin, K.-Y. A.; Ghanbari, F. Heterogeneous photocatalytic activation of electrogenerated chlorine for the production of reactive oxygen and chlorine species: A new approach for Bisphenol A degradation in saline wastewater. *J. Hazard. Mater.* **2023**, *445*, No. 130626.

(3) Biswal, L.; Nayak, S.; Parida, K. Recent progress on strategies for the preparation of 2D/2D MXene/g-C_3N_4 nanocomposites for photocatalytic energy and environmental applications. *Catal. Sci. Technol.* **2021**, *11*, 1222−1248.

(4) Nayak, S.; Parida, K. MgCr-LDH nanoplatelets as effective oxidation catalysts for visible light-triggered Rhodamine B degradation. *Catalysts* **2021**, *11*, 1072.

(5) Nayak, S.; Parida, K. Recent progress in LDH@ graphene and analogous heterostructures for highly active and stable photocatalytic and photoelectrochemical water splitting. *Chem. −Asian J.* **2021**, *16*, 2211−2248.

(6) Nayak, S.; Parida, K. Superactive NiFe-LDH/graphene nanocomposites as competent catalysts for water splitting reactions. *Inorg. Chem. Front.* **2020**, *7*, 3805−3836.

(7) Nayak, S.; Mohapatra, L.; Parida, K. Visible light-driven novel gC_3N_4/NiFe-LDH composite photocatalyst with enhanced photocatalytic activity toward water oxidation and reduction reaction. *J. Mater. Chem. A* **2015**, *3*, 18622−18635.

(8) Nayak, S.; Parida, K. Deciphering Z-scheme charge transfer dynamics in heterostructure NiFe-LDH/N-rGO/g-C_3N_4 nanocomposite for photocatalytic pollutant removal and water splitting reactions. *Sci. Rep.* **2019**, *9*, 2458.

(9) Nayak, S.; Parida, K. Dynamics of charge-transfer behavior in a plasmon-induced quasi-type-II p−n/n−n dual heterojunction in Ag@ Ag_3PO_4/g-C_3N_4/NiFe LDH nanocomposites for photocatalytic Cr (VI) reduction and phenol oxidation. *ACS Omega* **2018**, *3*, 7324−7343.

(10) Nayak, S.; Pradhan, A. C.; Parida, K. Topotactic transformation of solvated MgCr-LDH nanosheets to highly efficient porous MgO/$MgCr_2O_4$ nanocomposite for photocatalytic H_2 evolution. *Inorg. Chem.* **2018**, *57*, 8646−8661.

(11) Nayak, S.; Parida, K. Nanostructured CeO_2/MgAl-LDH composite for visible light induced water reduction reaction. *Int. J. Hydrogen Energy* **2016**, *41*, 21166−21180.

(12) Zhang, L.; Lin, C.-Y.; Zhang, D.; Gong, L.; Zhu, Y.; Zhao, Z.; Xu, Q.; Li, H.; Xia, Z. Guiding principles for designing highly efficient metal-free carbon catalysts. *Adv. Mater.* **2019**, *31*, No. 1805252.

(13) Barrio, J.; Volokh, M.; Shalom, M. Polymeric carbon nitrides and related metal-free materials for energy and environmental applications. *J. Mater. Chem. A* **2020**, *8*, 11075−11116.

(14) Zhang, J. S.; Chen, Y.; Wang, X. C. Two-dimensional covalent carbon nitride nanosheets: synthesis, functionalization, and applications. *Energy Environ. Sci.* **2015**, *8*, 3092−3108.

(15) Ong, W. J.; Tan, L. L.; Ng, Y. H.; Yong, S. T.; Chai, S. P. Graphitic carbon nitride (g-C_3N_4)-based photocatalysts for artificial photosynthesis and environmental remediation: are we a step closer to achieving sustainability? *Chem. Rev.* **2016**, *116*, 7159−7329.

(16) Nayak, S.; Parida, K. Superlative photoelectrochemical properties of 3D MgCr-LDH nanoparticles influencing towards photoinduced water splitting reactions. *Sci. Rep.* **2022**, *12*, 9264.

(17) Nayak, S.; Das, K. K.; Parida, K. Indulgent of the physiochemical features of MgCr-LDH nanosheets towards photodegradation process of methylene blue. *J. Colloid Interface Sci.* **2023**, *634*, 121−137.

(18) Hassani, A.; Faraji, M.; Eghbali, P. Facile fabrication of mpg-C_3N_4/Ag/ZnO nanowires/Zn photocatalyst plates for photodegradation of dye pollutant. *J. Photochem. Photobiol. A* **2020**, *400*, No. 112665.

(19) Hassani, A.; Eghbali, P.; Metin, Ö. Sonocatalytic removal of methylene blue from water solution by cobalt ferrite/mesoporous graphitic carbon nitride ($CoFe_2O_4$/mpg-C_3N_4) nanocomposites: response surface methodology approach. *Environ. Sci. Pollut. R.* **2018**, *25*, 32140−32155.

(20) Tan, S.; Xing, Z.; Zhang, J.; Li, Z.; Wu, X.; Cui, J.; Kuang, J.; Zhu, Q.; Zhou, W. Ti^{3+}-TiO_2/g-C_3N_4 mesostructured nanosheets heterojunctions as efficient visible-light-driven photocatalysts. *J. Catal.* **2018**, *357*, 90−99.

(21) Savateev, A.; Antonietti, M. Ionic carbon nitrides in solar hydrogen production and organic synthesis: exciting chemistry and economic advantages. *ChemCatChem* **2019**, *11*, 6166−6176.

(22) Schlomberg, H.; Kröger, J.; Savasci, G. k.; Terban, M. W.; Bette, S.; Moudrakovski, I.; Duppel, V.; Podjaski, F.; Siegel, R.; Senker, J. r.; Dinnebier, R. E.; Ochsenfeld, C.; Lotsch, B. V. Structural insights into poly (heptazine imides): a light-storing carbon nitride material for dark photocatalysis. *Chem. Mater.* **2019**, *31*, 7478−7486.

(23) Savateev, A.; Pronkin, S.; Epping, J. D.; Willinger, M. G.; Wolff, C.; Neher, D.; Antonietti, M.; Dontsova, D. Potassium poly (heptazine imides) from aminotetrazoles: Shifting band gaps of carbon nitride-like materials for more efficient solar hydrogen and oxygen evolution. *ChemCatChem* **2017**, *9*, 167−174.

(24) Savateev, A.; Tarakina, N. V.; Strauss, V.; Hussain, T.; ten Brummelhuis, K.; Sanchez Vadillo, J. M.; Markushyna, Y.; Mazzanti, S.; Tyutyunnik, A. P.; Walczak, R.; Oschatz, M.; Guldi, D. M.; Karton, A.; Antonietti, M. Potassium poly(Heptazine Imide): Transition metal-free solid-state triplet sensitizer in cascade energy transfer and [3+2]-cycloadditions. *Angew. Chem. Int. Ed.* **2020**, *59*, 15061−15068.

(25) Sahoo, S. K.; Teixeira, I. F.; Naik, A.; Heske, J.; Cruz, D.; Antonietti, M.; Savateev, A.; Kuehne, T. D. Photocatalytic water splitting reaction catalyzed by ion-exchanged salts of potassium poly(heptazine imide) 2D materials. *J. Phys. Chem. C* **2021**, *125*, 13749−13758.

(26) Yu, H.; Shi, R.; Zhao, Y.; Bian, T.; Zhao, Y.; Zhou, C.; Waterhouse, G. I.; Wu, L. Z.; Tung, C. H.; Zhang, T. Alkali-assisted synthesis of nitrogen deficient graphitic carbon nitride with tunable band structures for efficient visible-light-driven hydrogen evolution. *Adv. Mater.* **2017**, *29*, No. 1605148.

(27) Zhao, D.; Dong, C. L.; Wang, B.; Chen, C.; Huang, Y. C.; Diao, Z.; Li, S.; Guo, L.; Shen, S. Synergy of dopants and defects in graphitic carbon nitride with exceptionally modulated band structures for efficient photocatalytic oxygen evolution. *Adv. Mater.* **2019**, *31*, No. 1903545.

(28) Kröger, J.; Podjaski, F.; Savasci, G.; Moudrakovski, I.; Jiménez-Solano, A.; Terban, M. W.; Bette, S.; Duppel, V.; Joos, M.; Senocrate, A.; Dinnebier, R.; Ochsenfeld, C.; Lotsch, B. V. Conductivity mechanism in ionic 2D carbon nitrides: from hydrated ion motion to enhanced photocatalysis. *Adv. Mater.* **2022**, *34*, No. 2107061.

(29) Zhu, C.; Luo, X.; Liu, C.; Wang, Y.; Chen, X.; Wang, Y.; Hu, Q.; Wu, X.; Liu, B. Defect-rich ultrathin poly-heptazine-imide-framework nanosheets with alkali-ion doping for photocatalytic solar hydrogen and selective benzylamine oxidation. *Nano Res.* **2022**, *15*, 8760−8770.

(30) Wu, S.; Yu, H.; Chen, S.; Quan, X. Enhanced photocatalytic H_2O_2 production over carbon nitride by doping and defect engineering. *ACS Catal.* **2020**, *10*, 14380−14389.

(31) Dontsova, D.; Pronkin, S.; Wehle, M.; Chen, Z.; Fettkenhauer, C.; Clavel, G.; Antonietti, M. Triazoles: a new class of precursors for

https://doi.org/10.1021/acsomega.3c00150
ACS Omega 2023, 8, 11397−11405

the synthesis of negatively charged carbon nitride derivatives. *Chem. Mater.* **2015**, *27*, 5170−5179.
(32) Li, X.; Chen, X.; Fang, Y.; Lin, W.; Hou, Y.; Anpo, M.; Fu, X.; Wang, X. High-performance potassium poly(heptazine imide) films for photoelectrochemical water splitting. *Chem. Sci.* **2022**, *13*, 7541−7551.
(33) Nimbalkar, D. B.; Nguyen, V.-C.; Shih, C.-Y.; Teng, H. Melem-derived poly(heptazine imide) for effective charge transport and photocatalytic reforming of cellulose into H_2 and biochemicals under visible light. *Appl. Catal. B-Environ.* **2022**, *316*, No. 121601.
(34) Cao, S.; Shen, B.; Tong, T.; Fu, J.; Yu, J. 2D/2D heterojunction of ultrathin MXene/Bi_2WO_6 nanosheets for improved photocatalytic CO_2 reduction. *Adv. Funct. Mater.* **2018**, *28*, No. 1800136.
(35) Gu, W.; Lu, F.; Wang, C.; Kuga, S.; Wu, L.; Huang, Y.; Wu, M. Face-to-face interfacial assembly of ultrathin g-C_3N_4 and anatase TiO_2 nanosheets for enhanced solar photocatalytic activity. *ACS Appl. Mater. Interfaces* **2017**, *9*, 28674−28684.
(36) Yang, C.; Qin, J.; Xue, Z.; Ma, M.; Zhang, X.; Liu, R. Rational design of carbon-doped TiO_2 modified g-C_3N_4 via in-situ heat treatment for drastically improved photocatalytic hydrogen with excellent photostability. *Nano Energy* **2017**, *41*, 1−9.
(37) Wei, K.; Li, K.; Yan, L.; Luo, S.; Guo, H.; Dai, Y.; Luo, X. One-step fabrication of g-C_3N_4 nanosheets/TiO_2 hollow microspheres heterojunctions with atomic level hybridization and their application in the multi-component synergistic photocatalytic systems. *Appl. Catal. B-Environ.* **2018**, *222*, 88−98.
(38) Elbanna, O.; Fujitsuka, M.; Majima, T. g-C_3N_4/TiO_2 mesocrystals composite for H_2 evolution under visible-light irradiation and its charge carrier dynamics. *ACS Appl. Mater. Interfaces* **2017**, *9*, 34844−34854.
(39) Lin, Y.; Shi, H.; Jiang, Z.; Wang, G.; Zhang, X.; Zhu, H.; Zhang, R.; Zhu, C. Enhanced optical absorption and photocatalytic H_2 production activity of g-C_3N_4/TiO_2 heterostructure by interfacial coupling: A DFT+ U study. *Int. J. Hydrogen Energy* **2017**, *42*, 9903−9913.
(40) Biswal, L.; Nayak, S.; Parida, K. Rationally designed Ti_3C_2/N, S-TiO_2/g-C_3N_4 ternary heterostructure with spatial charge separation for enhanced photocatalytic hydrogen evolution. *J. Colloid Interface Sci.* **2022**, *621*, 254−266.
(41) Xu, Y.; Wang, S.; Yang, J.; Han, B.; Nie, R.; Wang, J.; Wang, J.; Jing, H. In-situ grown nanocrystal TiO_2 on 2D Ti_3C_2 nanosheets for artificial photosynthesis of chemical fuels. *Nano Energy* **2018**, *51*, 442−450.
(42) Gao, Y.; Wang, L.; Zhou, A.; Li, Z.; Chen, J.; Bala, H.; Hu, Q.; Cao, X. Hydrothermal synthesis of TiO_2/Ti_3C_2 nanocomposites with enhanced photocatalytic activity. *Mater. Lett.* **2015**, *150*, 62−64.
(43) Han, X.; An, L.; Hu, Y.; Li, Y.; Hou, C.; Wang, H.; Zhang, Q. Ti_3C_2 MXene-derived carbon-doped TiO_2 coupled with g-C_3N_4 as the visible-light photocatalysts for photocatalytic H_2 generation. *Appl. Catal. B-Environ.* **2020**, *265*, No. 118539.
(44) Chivu, V.; Gilea, D.; Cioatera, N.; Carja, G.; Mureseanu, M. Heterostructures of Ce-Ti/layered double hydroxides and the derived MMOs for photoenergy applications. *Appl. Surf. Sci.* **2020**, *513*, No. 145853.
(45) Madihi-Bidgoli, S.; Asadnezhad, S.; Yaghoot-Nezhad, A.; Hassani, A. Azurobine degradation using Fe2O3@ multi-walled carbon nanotube activated peroxymonosulfate (PMS) under UVA-LED irradiation: performance, mechanism and environmental application. *J. Environ. Chem. Eng.* **2021**, *9*, No. 106660.
(46) Ghidiu, M.; Lukatskaya, M. R.; Zhao, M.-Q.; Gogotsi, Y.; Barsoum, M. W. Conductive two-dimensional titanium carbide 'clay' with high volumetric capacitance. *Nature* **2014**, *516*, 78−81.
(47) Tang, R.; Xiong, S.; Gong, D.; Deng, Y.; Wang, Y.; Su, L.; Ding, C.; Yang, L.; Liao, C. Ti_3C_2 2D MXene: Recent progress and perspectives in photocatalysis. *ACS Appl. Mater. Interfaces* **2020**, *12*, 56663−56680.
(48) Lin, L.; Ren, W.; Wang, C.; Asiri, A.; Zhang, J.; Wang, X. Crystalline carbon nitride semiconductors prepared at different temperatures for photocatalytic hydrogen production. *Appl. Catal. B-Environ.* **2018**, *231*, 234−241.
(49) Wang, X.-J.; Yang, W.-Y.; Li, F.-T.; Xue, Y.-B.; Liu, R.-H.; Hao, Y.-J. In situ microwave-assisted synthesis of porous N-TiO_2/g-C_3N_4 heterojunctions with enhanced visible-light photocatalytic properties. *Ind. Eng. Chem. Res.* **2013**, *52*, 17140−17150.
(50) Tan, Y.; Shu, Z.; Zhou, J.; Li, T.; Wang, W.; Zhao, Z. One-step synthesis of nanostructured g-C_3N_4/TiO_2 composite for highly enhanced visible-light photocatalytic H_2 evolution. *Appl. Catal. B-Environ.* **2018**, *230*, 260−268.
(51) Wang, W.; Shu, Z.; Liao, Z.; Zhou, J.; Meng, D.; Li, T.; Zhao, Z.; Xu, L. Sustainable one-step synthesis of nanostructured potassium poly(heptazine imide) for highly boosted photocatalytic hydrogen evolution. *Chem. Eng. J.* **2021**, *424*, No. 130332.
(52) Zhang, G.; Xu, Y.; He, C.; Zhang, P.; Mi, H. Oxygen-doped crystalline carbon nitride with greatly extended visible-light-responsive range for photocatalytic H_2 generation. *Appl. Catal. B-Environ.* **2021**, *283*, No. 119636.
(53) Du, X.; Bai, X.; Xu, L.; Yang, L.; Jin, P. Visible-light activation of persulfate by TiO_2/g-C_3N_4 photocatalyst toward efficient degradation of micropollutants. *Chem. Eng. J.* **2020**, *384*, No. 123245.
(54) Yi, X.; Yuan, J.; Tang, H.; Du, Y.; Hassan, B.; Yin, K.; Chen, Y.; Liu, X. Embedding few-layer $Ti_3C_2T_x$ into alkalized g-C_3N_4 nanosheets for efficient photocatalytic degradation. *J. Colloid Interface Sci.* **2020**, *571*, 297−306.
(55) Shen, L.; Xing, Z.; Zou, J.; Li, Z.; Wu, X.; Zhang, Y.; Zhu, Q.; Yang, S.; Zhou, W. Black TiO_2 nanobelts/g-C_3N_4 nanosheets laminated heterojunctions with efficient visible-light-driven photocatalytic performance. *Sci. Rep.* **2017**, *7*, 41978.
(56) Liu, Y.; Xiao, H.; Goddard, W. A., III Schottky-barrier-free contacts with two-dimensional semiconductors by surface-engineered MXenes. *J. Am. Chem. Soc.* **2016**, *138*, 15853−15856.
(57) Shen, G.-D.; Pu, Y.-P.; Cui, Y.-F.; Jing, P.-P. Easy synthesis of TiO_2/g-C_3N_4 heterostructure photocatalyst with large surface area and excellent photocatalytic activity. *Ceram. Int.* **2017**, *43*, S664−S670.

https://doi.org/10.1021/acsomega.3c00150
ACS Omega 2023, 8, 11397−11405